

# Self-Discharge Behavior of Graphitic Cathodes for Rechargeable Aluminum Batteries

Chi Li, Yi-Xiu Chen, Jagabandhu Patra, Shi-Xian Lu, Chien-Te Hsieh, Chun-Chen Yang, Quan-Feng Dong, Ju Li, and Jeng-Kuei Chang\*

Self-discharge, which is associated with energy efficiency loss, is a critical issue that hinders practical applications of rechargeable aluminum batteries (RABs). The self-discharge properties of two commonly-used RAB positive electrode materials, namely natural graphite (NG) and expanded graphite (EG), are investigated in this work. EG, which has a wider spacing between graphitic layers and a larger surface area, has a higher self-discharge rate than that of NG. After 12 h of rest, NG and EG electrodes retain 74% and 63% of their initial capacities, respectively, after charging up to 2.4 V at 0.3 A g<sup>-1</sup>. Operando X-ray diffraction, X-ray photoelectron spectroscopy, and energy-dispersive X-ray spectroscopy are employed to study the self-discharge mechanism. The self-discharge loss is related to the spontaneous deintercalation of AlCl<sub>4</sub><sup>-</sup> anions from the graphite lattice charge-compensated by Cl<sub>2</sub> gas evolution at the same electrode and can be restored (i.e., no permanent damage is caused to the electrodes) in the next charge-discharge cycle. It is found that the charging rate and depth of charge also affect the self-discharge properties. In addition, the self-discharge rates of NG in 1-ethyl-3-methylimidazolium chloride–AlCl<sub>3</sub> and urea–AlCl<sub>3</sub> electrolytes are compared.

about fossil fuel depletion and climate change.<sup>[1,2]</sup> However, many sustainable energy sources are intermittent. Efficient energy storage is thus required to stabilize their power output.<sup>[3]</sup> Rechargeable batteries, which utilize reversible electrochemical reactions, are promising for modulating unstable energy owing to their high redox efficiency, flexibility, and versatility.<sup>[4,5]</sup> Although Li-ion batteries are commonly used, some drawbacks, such as the scarcity of Lithium (Li), Cobalt, and other required elements and safety issues related to the instability of the electrodes and electrolytes, limit their wide application. Rechargeable aluminum batteries (RABs) have emerged as a potential alternative to Li-ion batteries because Aluminum (Al) is highly abundant (Al and Li account for ≈8.21 wt% and ≈0.0065 wt% of the Earth's crust, respectively) and inexpensive (≈2000 USD per ton).<sup>[6–8]</sup> Al metal has a high volumetric capacity of 8040 mAh cm<sup>-3</sup>, which is about four times higher than that of Li metal.<sup>[9–11]</sup> Furthermore, it is eco-friendly and easy to handle even under air. Owing to the use of ionic liquid (IL) electrolytes, RABs are essentially not flammable or explosive and thus have minimal safety concerns.<sup>[12]</sup> The study of RABs is still in the early stages.

## 1. Introduction

Renewable energy, such as wind and solar energy, plays an important role in power generation because of increasing concerns

metal.<sup>[9–11]</sup> Furthermore, it is eco-friendly and easy to handle even under air. Owing to the use of ionic liquid (IL) electrolytes, RABs are essentially not flammable or explosive and thus have minimal safety concerns.<sup>[12]</sup> The study of RABs is still in the early stages.

C. Li, J. Patra, S.-X. Lu, J.-K. Chang  
Department of Materials Science and Engineering  
National Yang Ming Chiao Tung University  
1001 University Road, Hsinchu 30010, Taiwan  
E-mail: jkchang@nctu.edu.tw

C. Li, Y.-X. Chen, J.-K. Chang  
Institute of Materials Science and Engineering  
National Central University  
300 Zhong-Da Road, Taoyuan 32001, Taiwan

J. Patra, J.-K. Chang  
Hierarchical Green-Energy Materials (Hi-GEM) Research Center  
National Cheng Kung University  
1 University Road, Tainan 70101, Taiwan

C.-T. Hsieh  
Department of Chemical Engineering and Materials Science  
Yuan Ze University  
135 Yuandong Road, Taoyuan 32003, Taiwan

C.-C. Yang  
Battery Research Center of Green Energy  
Ming Chi University of Technology  
84 Gongzhuang Road, New Taipei City 243303, Taiwan

Q.-F. Dong  
State Key Laboratory for Physical Chemistry of Solid Surfaces  
Department of Chemistry  
Xiamen University  
422 South Siming Road, Xiamen 361005, China

J. Li  
Department of Nuclear Science and Engineering and Department of  
Materials Science and Engineering  
Massachusetts Institute of Technology  
77 Massachusetts Avenue, Cambridge, MA 02139, USA

J.-K. Chang  
Department of Chemical Engineering  
Chung Yuan Christian University  
200 Chung Pei Road, Taoyuan 32023, Taiwan

 The ORCID identification number(s) for the author(s) of this article can be found under <https://doi.org/10.1002/adfm.202305511>

DOI: 10.1002/adfm.202305511

Some redox mechanisms have not yet been fully clarified. Further development of RABs and a better understanding of the limiting factors, such as self-discharge properties, are required to realize the practical applications of RABs.

Significant progress has been achieved in the development of RAB cathodes, including those based on carbonaceous materials,<sup>[13–19]</sup> oxides,<sup>[20–23]</sup> chalcogenides,<sup>[24–27]</sup> chalcogens,<sup>[28–30]</sup> and organic materials.<sup>[31–34]</sup> Oxides and chalcogenides generally exhibit high specific capacities of 200–600 mAh g<sup>-1</sup> owing to multielectron redox transitions upon Al<sup>3+</sup> uptake/release. However, limited cycle life has been observed in most cases due to the strong Coulombic interaction between the high-charge-density Al<sup>3+</sup> and host materials, which leads to irreversible capacity degradation.<sup>[10,11,35]</sup> Chalcogen elements have high specific capacities: 1300–1600 mAh g<sup>-1</sup> for Sulfur,<sup>[28,29]</sup> 655 mAh g<sup>-1</sup> for Selenium,<sup>[28]</sup> and 935 mAh g<sup>-1</sup> for Tellurium.<sup>[30]</sup> Nonetheless, chalcogens often suffer from poor electronic conductivity,<sup>[30,35,36]</sup> severe structural collapse during charging/discharging, and the shuttle effect through the electrolyte, which lead to unsatisfactory electrode rate capability and cyclability.<sup>[10,11,35]</sup> Organic materials, which are lightweight, affordable, and molecularly designable, are interesting RAB cathodes.<sup>[11,31,32,35]</sup> Despite their promising features, some organic compounds easily swell and dissolve in the electrolyte, causing pronounced performance deterioration.<sup>[31,32]</sup> Carbonaceous materials, including various forms of graphitic substances, graphene nanosheets, mesoporous carbon, metal-organic-framework-derived carbon, and zeolite-templated carbon, are practically attractive because of their abundant reserves, great environmental compatibility, and high affordability.<sup>[13,18,19,37,38]</sup> The simple intercalation/deintercalation mechanism of AlCl<sub>4</sub><sup>-</sup> anions:  $x\text{AlCl}_4^- (\text{liquid electrolyte}) + \text{C}_n = \text{C}_n(\text{AlCl}_4)_x + xe^- (\text{current collector})$ , where the solid intercalation compound C<sub>n</sub>(AlCl<sub>4</sub>)<sub>x</sub> can be considered to consist of partially oxidized graphitic carbon surrounding mobile AlCl<sub>4</sub><sup>-</sup> (graphite), with the AlCl<sub>4</sub><sup>-</sup> (graphite) anions moving readily along the graphitic interstice due to their low charge density and thus low Coulombic interaction with the carbon hosts, gives most carbonaceous cathodes excellent rate capability and cyclability.<sup>[13,35]</sup> However, a major drawback of carbon-based cathodes, self-discharge, is often neglected and thus requires further investigation.

Self-discharge refers to the spontaneous reduction in the stored electrical energy after a battery rests in an open-circuit condition. It results in energy loss and a decrease in the charge-discharge Coulombic efficiency.<sup>[39]</sup> The self-discharge kinetics depends on the battery chemistry, electrode and electrolyte composition and design, impurities, and storage temperature.<sup>[40]</sup> The self-discharge loss of RABs<sup>[34,41]</sup> is much higher than that of commercial Li-ion batteries, which is typically a few percent per month.<sup>[42]</sup> RABs with graphitic cathodes usually show serious self-discharge.<sup>[34,43,44]</sup> Shi et al. reported that an Al//graphite cell had a higher capacity at a higher discharge rate.<sup>[45]</sup> At a low discharge current density, chemical self-discharge was predominant, reducing the electrochemical discharge capacity. Graphite electrodes in high-temperature inorganic molten salt electrolytes have also been reported to have a high self-discharge rate.<sup>[46,47]</sup> Even though self-discharge limits the practical applications of RABs, their behavior and reaction mechanism have not been clarified. In addition, the relation between the electrode mate-

rial properties and the self-discharge rate has not been examined. These issues are considered in this work. Generally speaking, the higher the *x* in C<sub>n</sub>(AlCl<sub>4</sub>)<sub>x</sub>, the more oxidized the graphitic carbons become (one can think of more electronic holes on the “C<sub>n</sub> part” of C<sub>n</sub>(AlCl<sub>4</sub>)<sub>x</sub>), and the more positive the graphitic electrode potential becomes. While it is easy to achieve large *x/n* due to the facile kinetics of AlCl<sub>4</sub><sup>-</sup> (graphite) intercalation, the graphitic lattice could over-engage so many AlCl<sub>4</sub><sup>-</sup> (graphite) anions that, at a certain point, the electronic holes on the C<sub>n</sub> part of C<sub>n</sub>(AlCl<sub>4</sub>)<sub>x</sub> could be used to drive a chlorine gas evolution reaction. This gassing would be accompanied by simultaneous disengagement of AlCl<sub>4</sub><sup>-</sup> (graphite) from the lattice, which reduces *x* and the open-circuit potential of the electrode, which is the self-discharge.

In the present study, the capacities, rate capability, and cycling stability of two common RAB cathodes, namely natural graphite (NG) and expanded graphite (EG), are systematically compared. Most importantly, the self-discharge behavior of the two cathodes is, for the first time, characterized in detail. Synchrotron operando X-ray diffraction (XRD), X-ray photoelectron spectroscopy (XPS), and energy-dispersive X-ray spectroscopy (EDS) mapping are employed to investigate the self-discharge mechanism. The effects of the lattice size and surface area of the cathode materials on the self-discharge rate and those of the charging rate, depth of charge, and IL electrolyte composition on the self-discharge properties are investigated.

## 2. Results and Discussion

The appearance and morphologies of NG and EG are shown in **Figure 1a–c**. NG shows a flake-like morphology with a lateral size of up to ≈150 μm, whereas EG shows a unique expanded and porous structure. **Figure 1d** shows the XRD patterns for the NG and EG samples. The pattern for the former has a sharp characteristic peak at 26.6°, which is associated with the (002) plane diffraction of graphite. The interlayer *d* spacing calculated according to Bragg's law is 3.35 Å. The pattern for the latter has a main diffraction peak at 26.2°, corresponding to a (002) *d* spacing of 3.40 Å. The larger interplane distance of the EG sample is related to the thermal expansion of the graphite intercalation compound precursor during synthesis.<sup>[48,49]</sup> The Raman spectra in **Figure 1e** show the *D* band (at ≈1355 cm<sup>-1</sup>) and *G* band (at ≈1580 cm<sup>-1</sup>) of the two carbon materials. The *D* band is associated with imperfect sp<sup>2</sup> carbon bonding and the *G* band results from the in-plane vibration of a well-ordered graphitic lattice.<sup>[50,51]</sup> The higher *D*-band intensity of EG indicates a higher disordered portion of carbon, which is attributed to the defects generated by the introduction of intercalants and their extraction from the graphite lattice upon the thermal expansion process.<sup>[48,49]</sup> The signal at ≈1750 cm<sup>-1</sup> for EG is related to its surface carboxyl groups. **Figure 1f** shows the N<sub>2</sub> adsorption/desorption data for the NG and EG samples. Both isotherms can be characterized as type III isotherms according to the International Union of Pure and Applied Chemistry denomination.<sup>[52]</sup> The calculated Brunauer–Emmett–Teller surface area values are 5.5 and 28.6 m<sup>2</sup> g<sup>-1</sup> for NG and EG, respectively.

**Figure 2a** shows the cyclic voltammetry (CV) curves for the NG and EG electrodes measured in the 1-ethyl-3-methylimidazolium chloride (EMICl)–AlCl<sub>3</sub> IL electrolyte with a potential scan rate of 1 mV s<sup>-1</sup>. The two electrodes exhibit similar redox behavior.

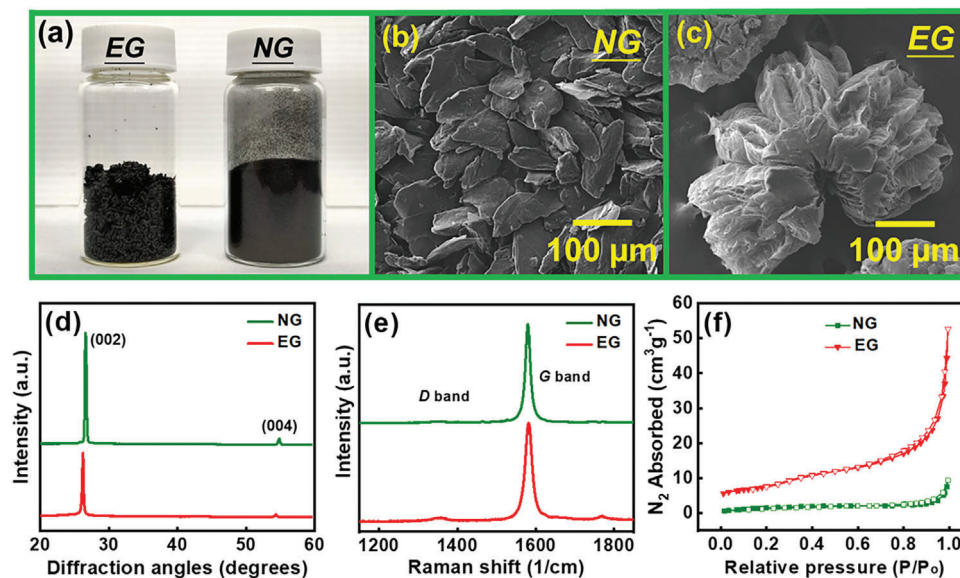


**Figure 1.** a) Appearance of NG and EG powder. SEM images of b) NG and c) EG samples. d) XRD patterns, e) Raman spectra, and f)  $N_2$  adsorption/desorption data of NG and EG samples.

During the positive scan, multiple anodic peaks associated with various stages of  $AlCl_4^-$  intercalation into the graphite lattice appear,<sup>[45,46]</sup> where the “ $C_n$  part” of  $C_n(AlCl_4)_x$  is oxidized with more delocalized holes. When the potential was scanned in the reverse direction, the deintercalation of  $AlCl_4^-$  ions and reduction of the “ $C_n$  part” occurred. The Coulombic efficiency of both electrodes was found to be  $\approx 99\%$ , indicating high reversibility of the charge storage reactions. The galvanostatic charge-discharge curves for the NG and EG electrodes are shown in Figure 2b,c, respectively. For the NG electrode, there are two clear potential plateaus, especially at a low charge-discharge rate (i.e., one at  $\approx 2.25$  V and one at below 1.85 V during discharging). For the EG electrode, these two plateaus are less pronounced, probably because the double-layer charging/discharging mechanism was more involved due to the higher surface area of EG.<sup>[53]</sup> The reversible capacities of NG and EG at  $0.3$  A  $g^{-1}$  are 85 and 95 mAh  $g^{-1}$ , respectively. As shown, they decrease to 28 and 46 mAh  $g^{-1}$ , respectively, at  $2$  A  $g^{-1}$ . EG has a larger  $d$  spacing and a higher surface area to accommodate more  $AlCl_4^-$  anions, leading to higher specific capacities. Figure 2d compares the rate capability of the two electrodes. The capacities of the NG and EG electrodes at  $2$  A  $g^{-1}$  are respectively 34% and 48% of the values measured at  $0.3$  A  $g^{-1}$ . The cause of the difference in the capacity retention at a high rate between the two electrodes was examined with electrochemical impedance spectroscopy (EIS). The Nyquist plots in Figure 2e are composed of a semicircle at high frequency and a sloping line at low frequency, which can be fitted using the equivalent circuit shown in the figure inset, where  $R_e$ ,  $R_{ct}$ ,  $CPE$ , and  $W$  are the electrolyte resistance, charge transfer resistance, interfacial constant-phase element, and Warburg impedance term, respectively.<sup>[54,55]</sup> It is found that the  $R_{ct}$  values, corresponding to the diameters of the EIS semicircles, are 18.0 and 14.5  $\Omega$ , respectively, for the NG and EG electrodes. The lower  $R_{ct}$  for EG can be attributed to its unique expanded and porous structure, which increases electrolyte accessibility and the num-

ber of reaction sites. Moreover, an enlarged and defective carbon lattice has been reported to promote ionic conduction.<sup>[18,56]</sup> These factors explain the superior rate capability of the EG electrode.

Figure 2f shows the cycling stability data of the two electrodes evaluated in the IL electrolyte. After 1000 charge-discharge cycles, the capacity retention was  $\approx 74\%$  and  $\approx 98\%$ , respectively, for the NG and EG electrodes. The clear capacity decay of the former electrode can be ascribed to the structural deterioration of NG. As shown in Figure S1, Supporting Information, the cycled NG electrode exhibits disintegration due to the large volume variation during charging/discharging. The intercalation/deintercalation of the huge  $AlCl_4^-$  anions caused exfoliation of the graphitic layers and pulverization of the NG particles,<sup>[57,58]</sup> leading to the marked capacity decrease. Similar observations have been reported in the literature.<sup>[54,57]</sup> In contrast, little structural deterioration was found for the EG electrode after cycling. This is probably associated with the relatively low stress generated during the repeated uptake/release of  $AlCl_4^-$  owing to the large  $d$  spacing and relatively porous structure of EG. No significant influence of the EG surface carboxyl groups (as indicated by Raman data in Figure 1e) on the electrochemical properties and cycling stability was observed.

The self-discharge rate is a critical factor for practical batteries. It is thus important to investigate the self-discharge behavior of RAB electrodes. **Figures 3a,b** show the self-discharge properties of the NG and EG electrodes, respectively. After charging up to 2.4 V at  $0.3$  A  $g^{-1}$ , the cell rested in the open-circuit condition for various durations (up to 36 h) and then was discharged at the same rate to 0.5 V. After a self-discharge cycle, the cell was subjected to two regular charge-discharge cycles before the next self-discharge cycle was executed. As shown, during the resting period, the potential for both types of electrodes continuously declined, implying a charge loss. The NG electrode remained at 2.25 V after 36 h, whereas the EG electrode retained at only

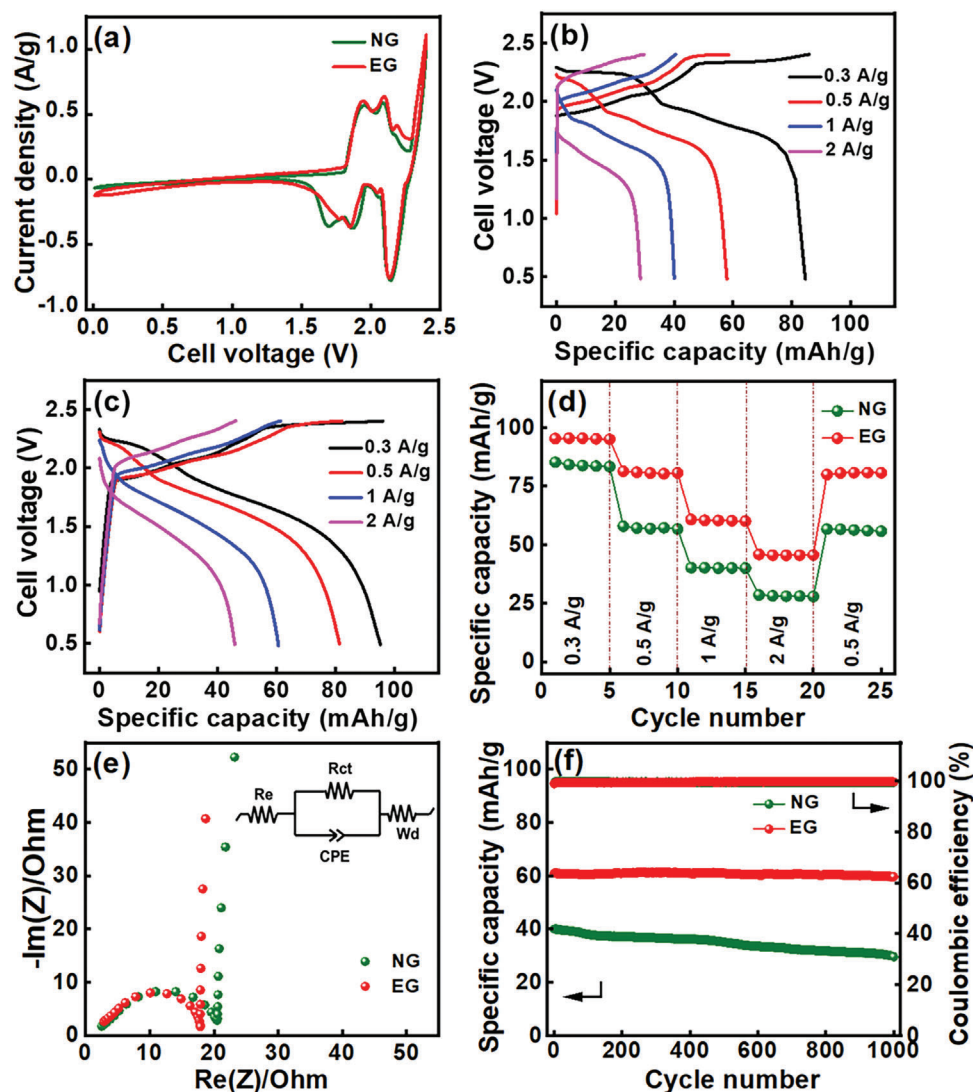


**Figure 2.** a) CV curves of NG and EG electrodes measured at a potential sweep rate of  $1 \text{ mV s}^{-1}$ . Galvanostatic charge-discharge curves of b) NG and c) EG electrodes. d) Comparison of reversible capacities of NG and EG electrodes measured at various rates. e) Nyquist spectra of NG and EG electrodes. f) Cycling stability data of NG and EG electrodes measured at  $1 \text{ A g}^{-1}$ .

1.99 V after the same time. The capacity retentions of the NG electrode after self-discharge time of 1, 2, 4, 8, 12, 24, and 36 h were 96%, 91%, 87%, 79%, 74%, 60%, and 56%, respectively; those of the EG electrode were 89%, 80%, 73%, 67%, 63%, 56%, and 53%, respectively. The experimental results indicate that the self-discharge rate of EG is higher than that of NG. This is partially associated with the fact that EG has a higher specific surface area and, thus, a larger double-layer capacitive contribution to the charge storage capacity. The double-layer capacitance easily self-discharges because the adsorbed ions on the electrode surface are readily redistributed and consumed when the applied power is removed.<sup>[59,60]</sup> The details of the self-discharge mechanisms of both electrodes are discussed later. Also shown in Figure 3 is that regardless of the electrode type, the charging curves almost overlap. Moreover, Figure S2, Supporting Information reveals that the measured discharge capacities of both electrodes do not change after the self-discharge cycles. These results confirm that the self-

discharge loss is restorable; no permanent damage is caused to the electrodes.

Figure 4a compares the discharge curves obtained before and after 8 h of self-discharge for the NG and EG electrodes. Interestingly, for both kinds of electrodes, the capacity loss is mainly related to the shortening of the upper plateau; the length of the lower plateau does not significantly change. For ease of discussion, the upper and lower plateaus are defined as illustrated in Figure S3, Supporting Information. Figure 4b,c show the retained capacities attributed to the upper and lower plateaus after various durations of self-discharge for the NG and EG electrodes, respectively. The retained capacities attributed to the upper plateau substantially decrease with time. They become almost zero after  $\approx 36$  and 24 h, respectively, for the NG and EG electrodes. However, the retained capacities attributed to the lower plateau basically remain unchanged for both electrodes. Figure 4d compares the upper-plateau capacity

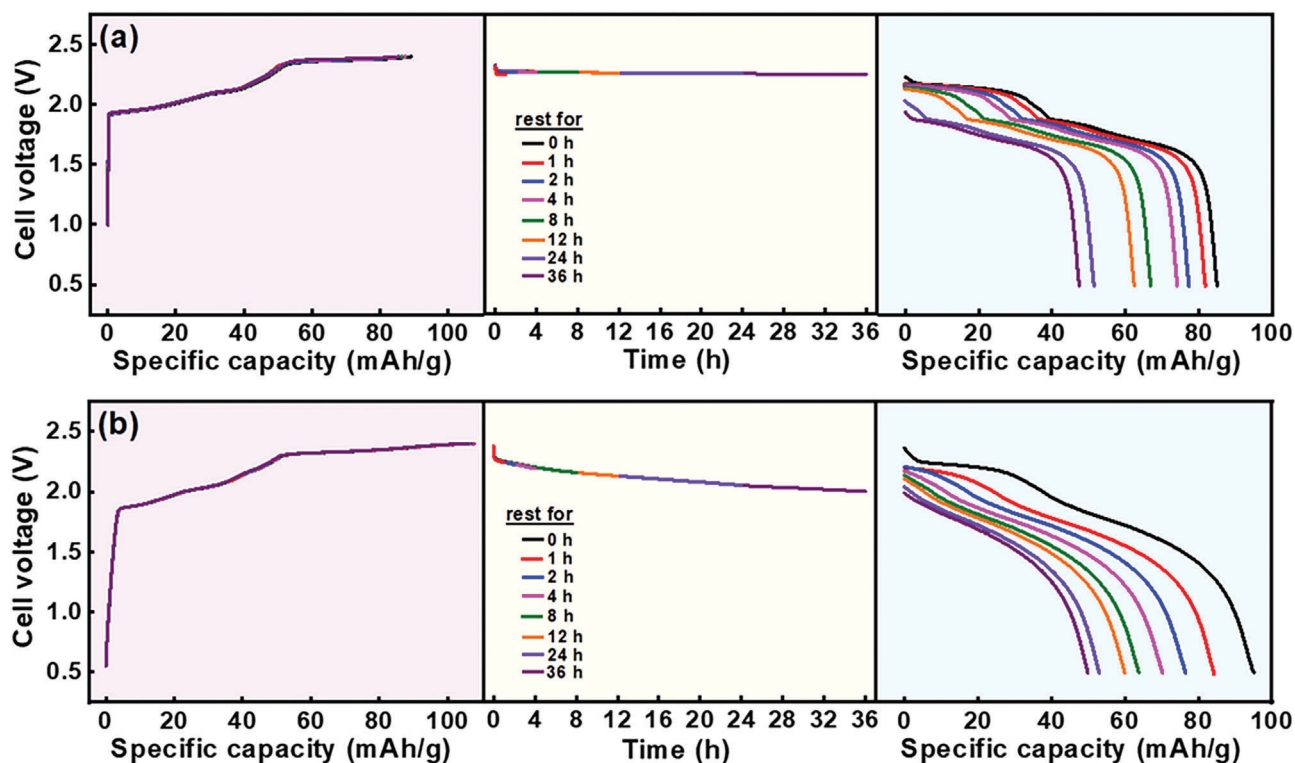


**Figure 3.** Self-discharge properties of a) NG and b) EG electrodes. After charging up to 2.4 V at  $0.3 \text{ A g}^{-1}$ , the cell rested in the open-circuit condition for various durations and then discharged at the same rate to 0.5 V.

retention ratios of the two electrodes after various periods of self-discharge. The capacity loss rate of EG is clearly higher than that of NG.

To investigate the self-discharge mechanism, operando XRD analyses were conducted during charging, self-discharging, and galvanostatic discharging. Due to the synchrotron beamtime restriction, a self-discharge time of 1 h was adopted. **Figure 5** shows the obtained series diffraction patterns for the NG electrode. Upon charging to 1.9 V, the pristine peak at  $26.6^\circ$  diminished, and two new peaks at  $\approx 24.2^\circ$  and  $\approx 27.6^\circ$  emerged. These two peaks moved farther apart, and the peak intensity increased when the cell was further charged to 2.4 V. These experimental results reflect the intercalation of  $\text{AlCl}_4^-$  anions into NG, which expands the graphitic interlayer.<sup>[12–14]</sup> The two new XRD peaks can be ascribed to (0 0  $n+1$ ) and (0 0  $n+2$ ) diffraction, respectively, where  $n$  represents the stage number of the graphite intercalation compound (GIC).<sup>[61]</sup> At 1.9 V, the calculated  $d_{(0\ 0\ n+1)}/d_{(0\ 0\ n+2)}$  ratio ( $3.645/3.227 \text{ \AA}$ ) is  $\approx 1.130$ , which corresponds to a stage-6 GIC (i.e., six free graphene planes between two anion-intercalated planes).<sup>[61,62]</sup> The stage numbers at various conditions were calculated from the XRD data. The results, shown in **Table 1**, indicate that a stage-4 GIC formed at the end of charging (i.e., at 2.4 V). As shown in **Figure 5**, during self-discharging, the two peaks shift in opposite directions (i.e., they move toward each other), suggesting that the  $\text{AlCl}_4^-$  anions were deintercalated from the graphite lattice. The stress of the graphitic layers after intercalation of the huge  $\text{AlCl}_4^-$  anions could be a driving force for spontaneous self-discharge. **Figure 5** also shows that

during the galvanostatic discharging, the two split XRD peaks gradually recombine into one peak, indicating a further release of  $\text{AlCl}_4^-$ .

**Table 1.** XRD data and stage numbers of NG cathode acquired using operando synchrotron XRD during charging, self-discharging, and discharging.

Potential [V]	$2\theta_{(0\ 0\ n+1)}$	$2\theta_{(0\ 0\ n+2)}$	$d_{(0\ 0\ n+1)}$ [Å]	$d_{(0\ 0\ n+2)}$ [Å]	$d_{(0\ 0\ n+1)}/d_{(0\ 0\ n+2)}$	Stage-X
1.9	24.21	27.60	3.645	3.227	1.130	6
2.0	24.07	27.69	3.665	3.217	1.139	6
2.1	23.71	27.91	3.718	3.194	1.164	5
2.2	23.56	28.03	3.727	3.175	1.174	5
2.3	23.38	28.16	3.767	3.168	1.189	4
2.4	23.30	28.20	3.780	3.164	1.195	4
10 min	23.32	28.18	3.776	3.166	1.193	4
20 min	23.34	28.14	3.774	3.170	1.190	4
30 min	23.35	28.03	3.773	3.180	1.186	4
40 min	23.36	27.99	3.771	3.186	1.184	4
50 min	23.38	27.98	3.769	3.186	1.183	4
60 min	23.39	27.97	3.766	3.188	1.181	4
2.0	23.40	27.95	3.764	3.190	1.180	4
1.8	23.70	27.86	3.719	3.199	1.163	5
1.6	24.36	27.41	3.624	3.274	1.107	7

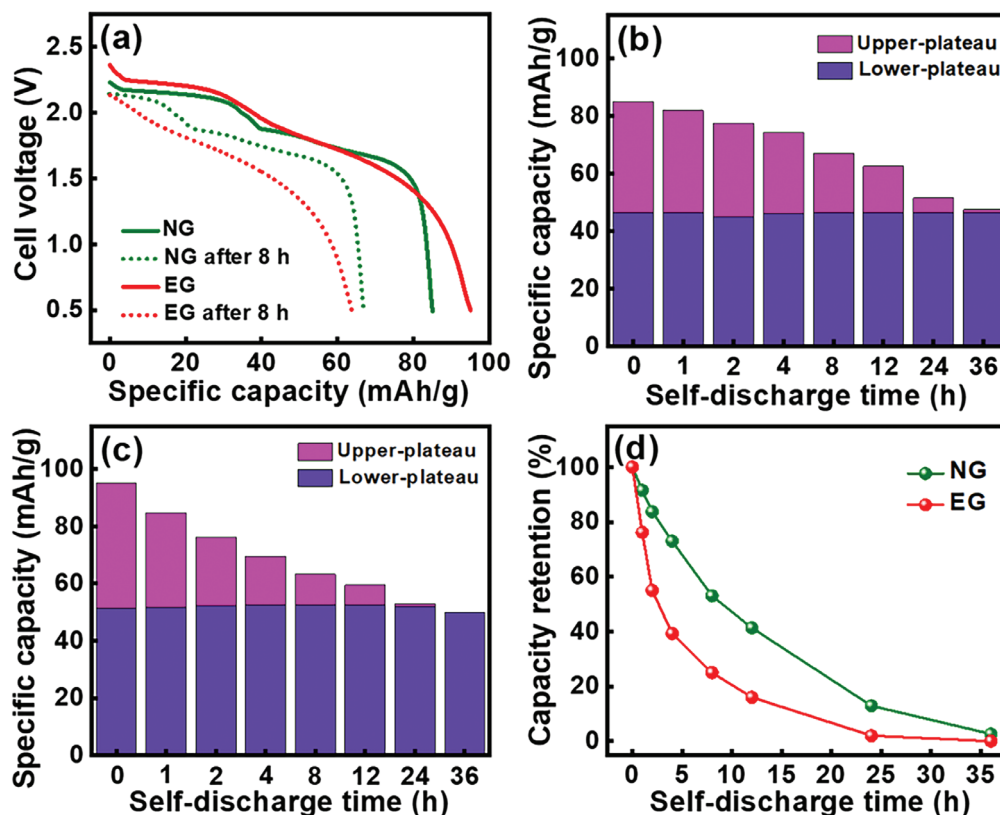


**Figure 4.** a) Discharge curves of NG and EG electrodes measured at  $0.3 \text{ A g}^{-1}$  before and after 8 h of self-discharge. Capacities attributed to upper and lower plateaus for b) NG and c) EG electrodes after various durations of self-discharge. d) Upper-plateau capacity retention ratios of NG and EG electrodes after various durations of self-discharge.

For the EG electrode, similar XRD characteristics corresponding to anion intercalation/deintercalation were found, as shown in **Figure 6**. Due to the difference in the crystallinity between NG and EG and the different synchrotron beamlines used for the two operando measurements, the signal-to-noise ratio is different for the two sets of XRD data. Nonetheless, a qualitative comparison between the two electrodes is still feasible. According to the calculation results listed in **Table 2**, a stage-4 GIC readily forms at 2.2 V, which is lower than that (2.3 V) for the NG electrode (**Table 1**) because the enlarged interlayer distance of EG facilitates the insertion of  $\text{AlCl}_4^-$  ions. Similar to the case for NG, in the open-circuit condition, the two split peaks shift toward each other, indicating the self-discharge of EG. After 1 h, the calculated  $d_{(00\ n+1)}/d_{(00\ n+2)}$  ratio is 1.152, which reflects a stage-5 GIC (rather than the stage-4 GIC after the same period of self-discharge for the NG electrode). These data confirm the faster self-discharge rate of the EG electrode found in the electrochemical measurements. The looser  $d$  spacing and more defects of the EG graphitic layers seem to be less favorable for holding intercalated  $\text{AlCl}_4^-$  anions, leading to a faster spontaneous anion release. As shown in **Figure 6**, when the cell is discharged back to 0.5 V, the two XRD peaks merge. It is noted that the peak position at the fully discharged state is more recovered compared to that for the NG electrode. This indicates that there were fewer trapped intercalants and/or less residual strain in the EG struc-

ture, confirming that the  $\text{AlCl}_4^-$  ions more easily escaped from the expanded carbon lattice.

It is thought that the charge compensation reactions for the anion-loss electrode reduction are those of the following oxidative decomposition of the species in the IL electrolyte.<sup>[11,63,64]</sup>



The anodic reactions (Equations (1)–(3)) at high enough electrode potential are responsible for the self-discharge phenomena. Note that the electrons released after the chlorine gas evolution will combine with the aforementioned electronic holes on the partially oxidized “ $\text{C}_n$  part” of  $\text{C}_n(\text{AlCl}_4)_x$ , and this, in turn, will drive out  $\text{AlCl}_4^-$  from the graphite lattice and reduce  $x$ . The higher surface area of EG (compared to that of NG) provides more sites for these interactions, which could promote self-discharge.

To further examine the self-discharge mechanism, XPS was used to investigate the electrode chemical states in the fully charged, self-discharged for 4 h, self-discharged for 12 h, and fully discharged conditions. **Figure 7a** shows the obtained data for the NG electrode. In the C 1s spectrum, besides the C–C bond-

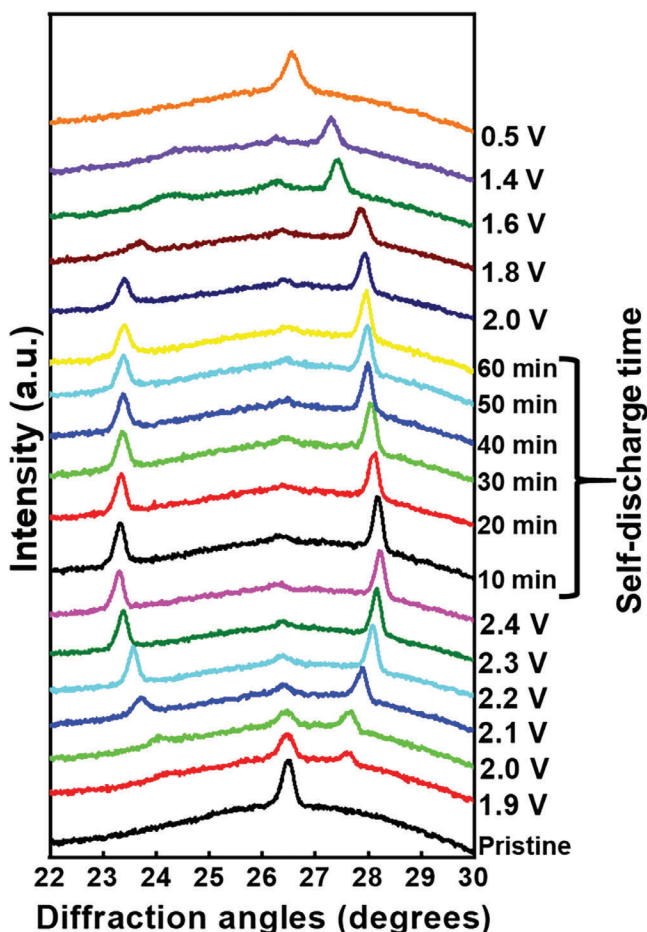


**Figure 5.** Operando synchrotron XRD patterns of NG cathode taken at various charge-discharge potentials and self-discharge states.

**Table 2.** XRD data and stage numbers of EG cathode acquired using operando synchrotron XRD during charging, self-discharging, and discharging.

Potential [V]	$2\theta_{(00\ n+1)}$	$2\theta_{(00\ n+2)}$	$d_{(00\ n+1)}$ [Å]	$d_{(00\ n+2)}$ [Å]	$d_{(00\ n+1)}/d_{(00\ n+2)}$	Stage-X
1.9	23.98	27.56	3.678	3.231	1.138	6
2.0	23.71	27.88	3.715	3.197	1.162	5
2.1	23.63	28.04	3.719	3.180	1.169	5
2.2	23.56	28.15	3.727	3.169	1.176	4
2.3	23.48	28.21	3.752	3.163	1.186	4
2.4	23.41	28.27	3.763	3.157	1.192	4
10 min	23.43	28.19	3.760	3.165	1.188	4
20 min	23.47	28.12	3.754	3.172	1.180	4
30 min	23.52	28.03	3.746	3.181	1.178	4
40 min	23.61	27.96	3.733	3.189	1.170	5
50 min	23.72	27.90	3.716	3.195	1.163	5
60 min	23.85	27.78	3.697	3.208	1.152	5
2.0	24.02	27.65	3.673	3.221	1.140	6
1.8	24.50	27.47	3.605	3.241	1.112	7
1.6	24.63	27.38	3.587	3.251	1.103	7

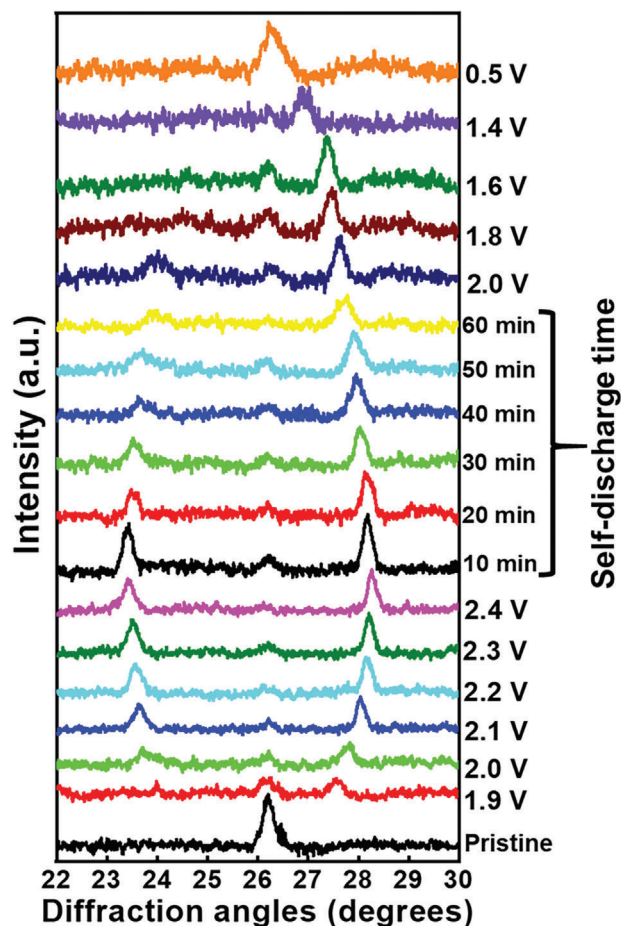


**Figure 6.** Operando synchrotron XRD patterns of EG cathode taken at various charge-discharge potentials and self-discharge states.

ing signal at  $\approx 284.6$  eV, a clear new shoulder peak at  $\approx 286.0$  eV appears in the fully charged state. This is associated with the oxidation of the NG electrode, which is charge-compensated by the intercalation of  $\text{AlCl}_4^-$  ions.<sup>[13,14]</sup> Upon charging, electrons are withdrawn by an external energy source, leading to electron deficiency of the graphite electrode. As a result, a blue shift in the binding energy of C1s was observed. In addition, a previous Bader charge analysis suggested that a significant amount of electron transfers from the C atoms to the Cl atoms of the  $\text{AlCl}_4$  molecules.<sup>[65]</sup> This also indicates the electrochemical oxidation of graphite due to  $\text{AlCl}_4$  intercalation. The insertion of chloroaluminate anions into NG after charging is also confirmed via the strong Al 2p and Cl 2p signals. However, after rest in the open-circuit condition, the C 1s shoulder and the Al and Cl peaks diminish with time, indicating the spontaneous deintercalation of  $\text{AlCl}_4^-$  from the carbon lattice. It is noted that the Al  $2p_{1/2}$  and  $2p_{3/2}$  signals are too close to be clearly distinguished, particularly for the intercalated  $\text{AlCl}_4^-$  anions, which are distorted in between the graphite layers, resulting in the broadening of the XPS signals. A similar XPS trend is found for the EG electrode, as shown in Figure 7b. However, a higher C 1s shoulder intensity compared to that of NG is observed after charging, which corresponds to the higher specific capacity (and thus more intercalated

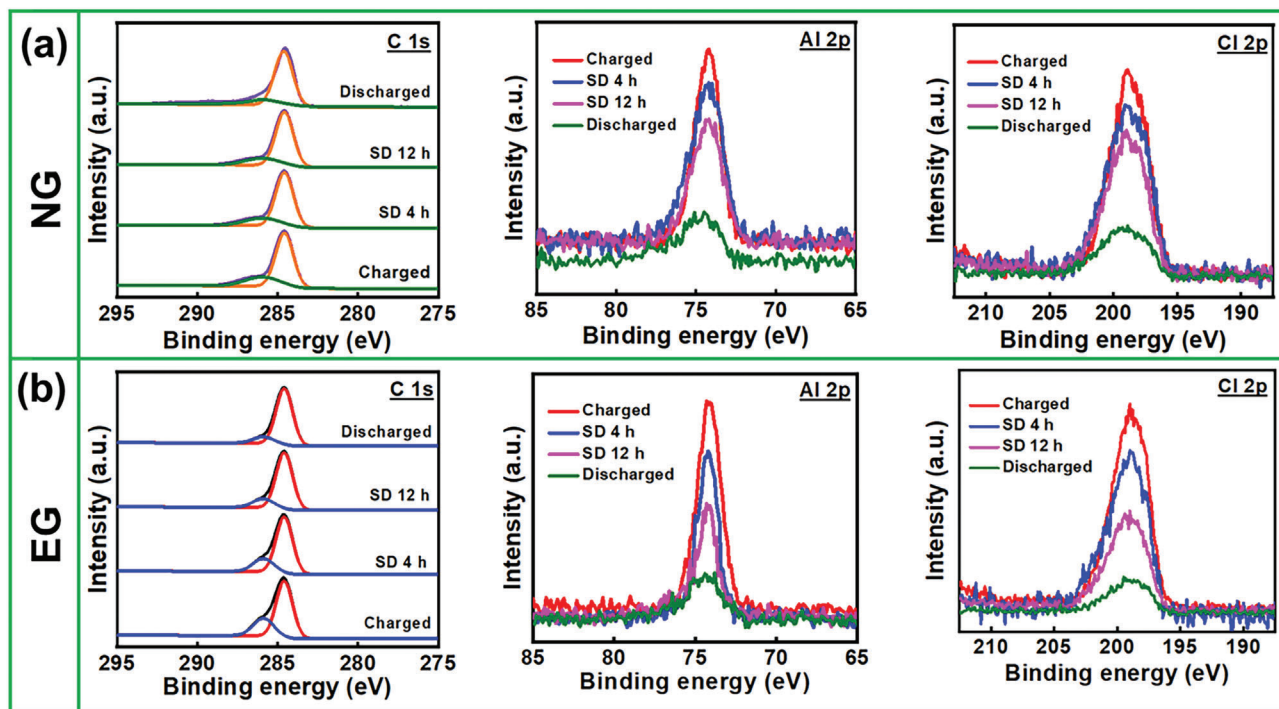


**Figure 7.** XPS C 1s, Cl 2p, and Al 2p spectra of a) NG and b) EG electrodes at fully charged, self-discharged of 4 h (SD 4 h), self-discharged of 12 h (SD 12 h), and fully discharged states.

$\text{AlCl}_4^-$  ions) of EG (see Figure 2). Of note, the C 1s shoulder and the Al and Cl peak intensity rapidly fade during rest in the open-circuit condition, confirming the higher self-discharge of the EG electrode.

Figure 8a,b show EDS mapping data for the NG and EG electrodes, respectively. In the charged state, the Al and Cl elements are uniformly distributed over both electrodes, reflecting the intercalation of  $\text{AlCl}_4^-$  ions. The higher Al and Cl concentrations of the EG electrode compared to those of the NG electrode can be attributed to the higher charge storage capacity of the former. It is noted that the Al and Cl intensities for the NG electrode, compared to those for the EG electrode, decrease more slowly during rest in the open-circuit condition, indicating a lower self-discharge rate. The smaller  $d$  spacing, fewer defects, and lower surface area of NG suppress the spontaneous release of the inserted  $\text{AlCl}_4^-$ , mitigating self-charge. In the fully discharged state, stronger signals from the remaining Al and Cl are observed for the NG electrode. These results are consistent with the operando XRD data and confirm the more difficult removal of  $\text{AlCl}_4^-$  ions from the NG lattice.

The self-discharge rate is altered by the operation conditions. Figure S4a, Supporting Information shows the effects of charging rate on the self-discharge properties of the NG electrode. For a rest of 12 h in the open-circuit condition, the self-discharge was mainly attributed to the capacity loss of the upper plateau regardless of the charging rate (the lower plateau basically remained unchanged, Figure S4b, Supporting Information). As shown, a high charging current density leads to a more pronounced shortening of the upper plateau length after self-discharge. Figure S4c, Supporting Information reveals that at a charging rate of

$50 \text{ mA g}^{-1}$ ,  $\approx 80\%$  of the capacity attributed to the upper plateau can be retained after a rest of 12 h in the open-circuit condition. However, at a charging rate of  $300 \text{ mA g}^{-1}$ , only  $\approx 45\%$  of the capacity attributed to the upper plateau can be retained after the same period of rest. With a higher current density, the intercalated  $\text{AlCl}_4^-$  ions have less time to be settled down at energy-favorable sites. Presumably, this gives rise to easier charge dissipation for the electrode.

The influence of the depth of charge on the self-discharge properties was also examined. The data for the NG electrode obtained at a charging rate of  $300 \text{ mA g}^{-1}$  are shown in Figure S5, Supporting Information. As shown, a higher depth of charge led to higher capacity loss attributed to the upper plateau. This is associated with the higher concentration of intercalated  $\text{AlCl}_4^-$ , creating a stronger driving force for self-discharge. As shown, the overall capacity retention ratio after 12 h of self-discharge increases with decreasing depth of charge. This is also associated with the fact that the lower plateau is almost immune to self-discharge.

Besides EMICl, urea was mixed with  $\text{AlCl}_3$  to form an IL analog electrolyte for RABs.<sup>[12,66]</sup> The self-discharge properties of the NG electrode in the urea- $\text{AlCl}_3$  electrolyte were also studied. The obtained experimental results are shown in Figure S6, Supporting Information. Because the urea- $\text{AlCl}_3$  electrolyte does not allow for fast charging/discharging, a relatively small current density of  $100 \text{ mA g}^{-1}$  was adopted. The reversible capacity obtained with the urea- $\text{AlCl}_3$  electrolyte is lower than that obtained with the EMICl- $\text{AlCl}_3$  electrolyte because of the higher viscosity and inferior ionic conductivity of the former electrolyte.<sup>[66]</sup> As shown in Figure S6, Supporting Information, with the urea- $\text{AlCl}_3$  electrolyte, the self-discharge also mainly happens for the

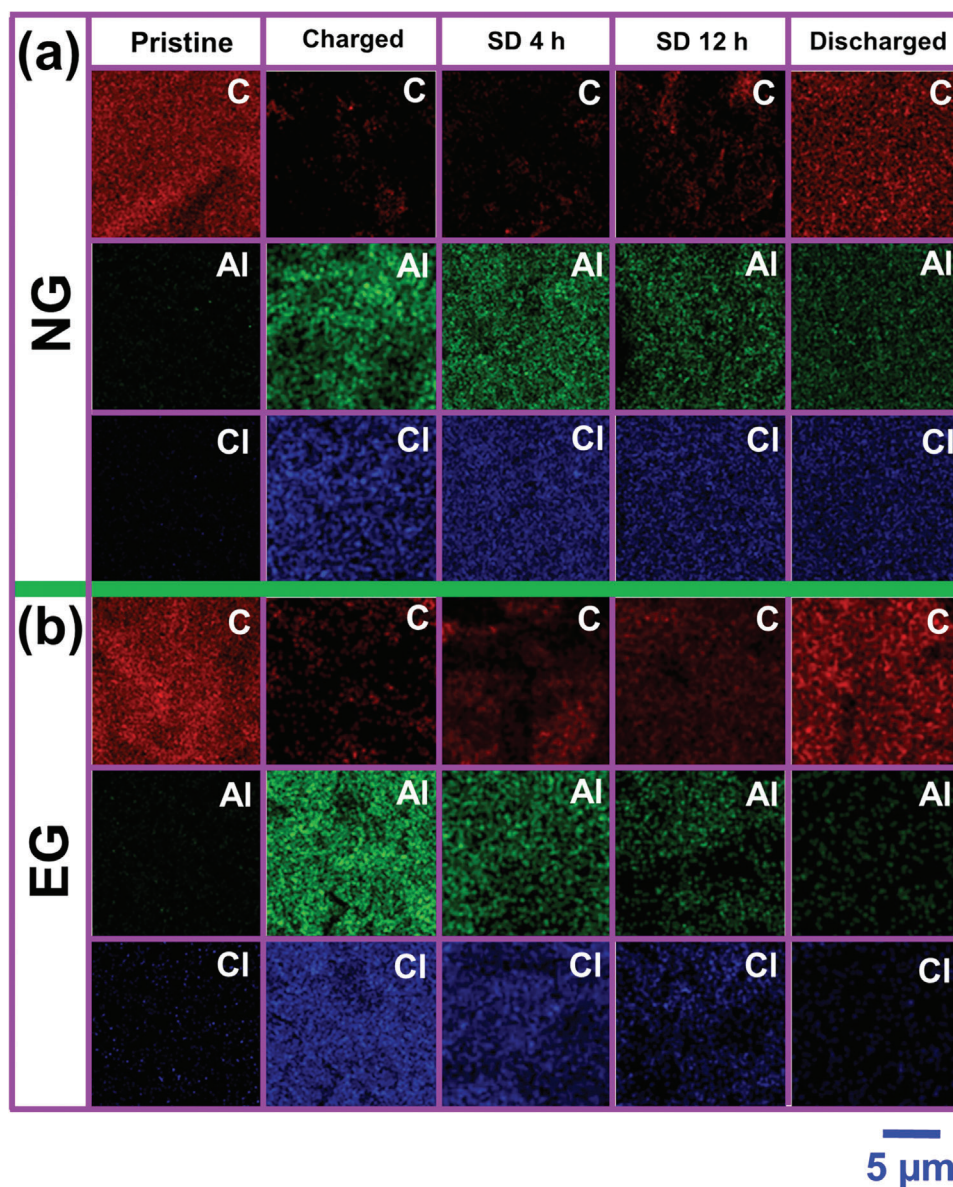


**Figure 8.** EDS mapping data of a) NG and b) EG electrodes at pristine, fully charged, self-discharged of 4 h (SD 4 h), self-discharged of 12 h (SD 12 h), and fully discharged states.

upper discharge plateau, suggesting that the proposed mechanism could be universal for graphitic RAB electrodes in various electrolytes. This figure also shows that the NG electrode has a higher self-discharge rate in urea- $\text{AlCl}_3$  compared to that in the EMICl- $\text{AlCl}_3$  electrolyte. After 12 h of self-discharge, the capacity retention ratio was only  $\approx 55\%$  in urea- $\text{AlCl}_3$ , which is much lower than the  $\approx 90\%$  in EMICl- $\text{AlCl}_3$  under the same experimental conditions. It has been reported that a stage-2 GIC forms after an electrode in the urea- $\text{AlCl}_3$  electrolyte is fully charged.<sup>[12]</sup> The higher intercalation degree, compared to the stage-4 GIC in EMICl- $\text{AlCl}_3$ , could induce more strain, which is prone to promote charge release upon resting. The narrower potential stability window of the urea- $\text{AlCl}_3$  electrolyte (i.e., anion deintercalation is encouraged by the electrolyte oxidative decomposition) may also contribute to the higher self-discharge rate. Electrolyte

modification can thus be an effective strategy for alleviating the self-discharge of RABs.

A key issue is the fate of the  $\text{Cl}_2$  gas produced by Equations (1)–(3). A lot of accumulated  $\text{Cl}_2$  gas would certainly be hazardous. But it is at least in principle possible for chlorine gas evolution reaction/chlorine gas reduction reaction to occur reversibly on the  $\text{C}_n(\text{AlCl}_4)_x$  electrode (reversing Equations (1)–(3)) and contribute some reversible capacity. Indeed some recent works point to this direction, where the  $\text{Cl}_2$  may exist as  $\text{Cl}_{2(\text{gas})}$  bubble or surface-adsorbed  $\text{Cl}_2^*$  and contribute some electrical energy.<sup>[67]</sup> Yet another possibility is that the  $\text{Cl}_2$  may have finite solubility in the liquid electrolyte, existing as  $\text{Cl}_{2(\text{liquid electrolyte})}$  in addition to the ionic form  $\text{Cl}^-_{(\text{liquid electrolyte})}$ , and cross over to the Al metal counter-electrode through the liquid bulk and recombine at the counter-electrode to form chloroaluminate ions<sub>(liquid electrolyte)</sub>. This route

would truly relax the chemical energy of the system, preventing unlimited  $\text{Cl}_2$  gas accumulation and unlimited decomposition of the liquid electrolyte. Such a redox-shuttle mechanism (weak  $\text{Cl}_{2(\text{liquid electrolyte})}$  solubility in addition to the  $\text{Cl}^-_{(\text{liquid electrolyte})}$  is equivalent to weak electronic leakage through the electrolyte) can self-discharge the battery until all the accumulated  $\text{Cl}_2$  on the  $\text{C}_n(\text{AlCl}_4)_x$  side, whether as  $\text{Cl}_{2(\text{gas})}$  or surface-adsorbed  $\text{Cl}_2^*$ , are gone. Even though one loses some electrical energy this way, it has better safety characteristics than keeping the accumulated  $\text{Cl}_2$  gas on the positive-electrode side. Clearly, the redox shuttle depends on the base electrolyte composition, whereas the  $\text{Cl}_{2(\text{gas})}/\text{Cl}_2^*$  storage characteristics depend on the details of the graphitic carbon, with both influencing the long-term self-discharge behavior.

### 3. Conclusion

Self-discharge is a crucial issue that needs to be addressed for RABs. The EG cathode showed a higher self-discharge rate than that of the NG cathode. After a rest of 12 h in the open-circuit condition, the NG and EG electrodes retained 74% and 63% of their initial capacities, respectively, after charging up to 2.4 V at  $0.3 \text{ A g}^{-1}$ . The upper plateau decay is mainly responsible for the capacity loss; the lower plateau basically remains unchanged. It was found that increasing the charging rate or depth of charge increased the self-discharge rate. The operando XRD, XPS, and EDS mapping data indicate that the self-discharge loss is related to the spontaneous deintercalation of  $\text{AlCl}_4^-$  anions from the graphite lattice, which is charge-compensated by the oxidative decomposition of the IL electrolyte. A different electrolyte composition was found to produce different self-discharge properties. Thus, electrolyte modification may be an effective strategy for alleviating the self-discharge of RABs. Regarding the electrode material, although increasing the  $d$  spacing and defect density of graphitic cathodes can improve the capacity and rate capability of RABs, the effect on the self-discharge rate should be monitored. In addition, a low specific surface area is recommended because it reduces the double-layer capacitance loss and the number of active sites for electrolyte decomposition, mitigating the electrode self-discharge.

### 4. Experimental Section

An IL electrolyte was prepared by slowly adding  $\text{AlCl}_3$  (99 wt%, Alfa Aesar) into EMICl (97 wt%, Acros) in an argon-filled glove box (Vigor Tech. Co. Ltd.), where both the moisture and oxygen content levels were maintained at  $\approx 0.1$  ppm. The molar ratio of  $\text{AlCl}_3$  to EMICl was 1.3:1. The mixture was continuously stirred by a magnetic paddle for 24 h to ensure uniformity. A cathode slurry was prepared by mixing 90 wt% NG or EG powder (both obtained from the Industrial Technology Research Institute, Taiwan) and 10 wt% poly(vinylidene fluoride) in *N*-methyl-2-pyrrolidone solvent. This slurry was agitated at 500 rpm for 2 h and then coated onto a carbon-fiber substrate. The electrode was dried at  $90^\circ\text{C}$  for 6 h to remove the *N*-methyl-2-pyrrolidone solvent. The active material loading was  $\approx 6 \text{ mg cm}^{-2}$ . An Al metal sheet and an Al metal strip were used as the counter and reference electrodes, respectively, in a three-electrode cell. The cell assembly and testing were done in the argon-filled glove box.

XRD (Bruker D8 Advance with a Cu target) was used to analyze the crystal structures. The X-ray detector was scanned at a speed of  $1^\circ \text{ min}^{-1}$ . The morphology and chemical composition of the samples were examined us-

ing SEM (FEI Inspect F50) and the auxiliary EDS, respectively. A Raman spectrometer (UniRAM MicroRaman with a laser wavelength of 532 nm) was employed to study the carbon bonding characteristics. The  $\text{N}_2$  adsorption/desorption experiments were conducted at  $-196^\circ\text{C}$  using a Micromeritics ASAP 2020 analyzer. The specific surface area was calculated based on the Brunauer–Emmett–Teller model. XPS (VG Sigma Probe) was used to study the chemical states of various electrodes. CV was performed with a potentiostat (Biologic VSP-300) at a potential sweep rate of  $1 \text{ mV s}^{-1}$  to characterize the electrochemical properties of the electrodes. The charge-discharge performance (in terms of capacity, rate capability, and cycling stability) of the cells was evaluated. EIS measurements were carried out in a frequency range of  $10^6$ – $10^{-2}$  Hz with a potential amplitude of 10 mV. All the electrochemical measurements were conducted at  $25^\circ\text{C}$ .

For the operando XRD analyses, pouch cells with an NG or EG positive electrode were used. Al foil ( $\approx 15 \mu\text{m}$  in thickness) and a glass-fiber membrane were used as the negative electrode and separator, respectively. The windows on both sides of the pouch cell for X-ray penetration were covered by Kapton tape. The cells were subjected to synchrotron XRD inspection, which was performed at Beamlines 01C and 17A at the National Synchrotron Radiation Research Center, Taiwan, during charging, self-discharging, and then discharging. The 2D diffraction signals were collected using an image plate detector (marXperts Mar345) and converted to 1D patterns using the software package Fit2D.

**Statistical Analysis:** The CV, EIS, charge-discharge, and self-discharge measurements of NG and EG electrodes were repeated at least five times to ensure validity. The performance deviation was typically within  $\approx 5\%$ , and the reported data were the medians. All the XPS spectra were calibrated with the binding energy of C 1s at 284.6 eV. The XPS data fitting was performed using XPSPEAK 4.1 software. The Origin software was used for data analysis and processing.

### Supporting Information

Supporting Information is available from the Wiley Online Library or from the author.

### Acknowledgements

The financial support provided for this work by the National Science and Technology Council (NSTC) of Taiwan is gratefully appreciated.

### Conflict of Interest

The authors declare no conflict of interest.

### Data Availability Statement

The data that support the findings of this study are available from the corresponding author upon reasonable request.

### Keywords

interlayer spacing, ionic liquid electrolytes, operando X-ray diffraction, potential plateau, surface areas

Received: May 17, 2023

Revised: June 28, 2023

Published online:

[1] M. Armand, J. M. Tarascon, *Nature* **2008**, 451, 652.

- [2] J. M. Tarascon, M. Armand, *Nature* **2001**, 414, 359.
- [3] H. Ibrahim, A. Ilinca, J. Perron, *Renewable Sustainable Energy Rev.* **2008**, 12, 1221.
- [4] D. Kundu, E. Talaie, V. Duffort, L. F. Nazar, *Angew. Chem., Int. Ed.* **2015**, 54, 3431.
- [5] J. B. Goodenough, K. S. Park, *J. Am. Chem. Soc.* **2013**, 135, 1167.
- [6] S. K. Das, *Angew. Chem., Int. Ed.* **2018**, 57, 16606.
- [7] H. Yang, H. Li, J. Li, Z. Sun, K. He, H. M. Cheng, F. Li, *Angew. Chem., Int. Ed.* **2019**, 58, 11978.
- [8] J. Chen, D. H. C. Chua, P. S. Lee, *Small Methods* **2020**, 4, 1900648.
- [9] G. A. Elia, K. Marquardt, K. Hoepfner, S. Fantini, R. Lin, E. Knipping, W. Peters, J. F. Drillet, S. Passerini, R. Hahn, *Adv. Mater.* **2016**, 28, 7564.
- [10] F. Wu, H. Yang, Y. Bai, C. Wu, *Adv. Mater.* **2019**, 31, 1806510.
- [11] J. Tu, W. L. Song, H. Lei, Z. Yu, L. L. Chen, M. Wang, S. Jiao, *Chem. Rev.* **2021**, 121, 4903.
- [12] M. Angell, C. J. Pan, Y. Rong, C. Yuan, M. C. Lin, B. J. Hwang, H. J. Dai, *Proc. Natl. Acad. Sci. U. S. A.* **2017**, 114, 834.
- [13] M. C. Lin, M. Gong, B. Lu, Y. Wu, D. Y. Wang, D. M. Guan, M. Angell, C. Chen, J. Yang, B. J. Hwang, H. J. Dai, *Nature* **2015**, 520, 324.
- [14] C. J. Pan, C. Yuan, G. Zhu, Q. Zhang, C. J. Huang, M. C. Lin, M. Angell, B. J. Hwang, P. Kaghazchi, H. J. Dai, *Proc. Natl. Acad. Sci. U. S. A.* **2018**, 115, 5670.
- [15] X. Dong, H. Chen, H. Lai, L. Wang, J. Wang, W. Fang, C. Gao, *J. Energy Chem.* **2022**, 66, 38.
- [16] X. Yu, B. Wang, D. Gong, Z. Xu, B. Lu, *Adv. Mater.* **2017**, 29, 1604118.
- [17] H. Huang, F. Zhou, P. Lu, X. Li, P. Das, X. Feng, K. Müllen, Z. S. Wu, *Energy Storage Mater.* **2020**, 27, 396.
- [18] P. Thanwisai, N. Chaiyapo, P. Phuenghinlad, Y. Kanaphan, J. Nash, C. Chotsuwan, A. Klamchuen, Y. Wang, T. Nann, N. Meethong, *Carbon* **2022**, 191, 195.
- [19] C. Li, P. C. Rath, S. X. Lu, J. Patra, C. Y. Su, D. Bresser, S. Passerini, J. K. Chang, *Chem. Eng. J.* **2021**, 417, 129131.
- [20] X. Zhang, G. Zhang, S. Wang, S. Li, S. Jiao, *J. Mater. Chem. A* **2018**, 6, 3084.
- [21] H. Lu, Y. Wan, T. Wang, R. Jin, P. Ding, R. Wang, Y. Wang, C. Teng, L. Li, X. Wang, D. Zhou, G. Xue, *J. Mater. Chem. A* **2019**, 7, 7213.
- [22] P. Almodovar, D. Giraldo, C. D. Guerra, J. R. Castellanos, J. M. G. Calbet, J. Chacon, M. L. Lopez, *J. Power Sources* **2021**, 516, 230656.
- [23] S. Ju, J. Ye, Y. Meng, G. Xia, X. Yu, *Adv. Energy Mater.* **2022**, 12, 2201653.
- [24] Y. Du, B. Zhang, W. Zhang, H. Jin, J. Qin, J. Wan, J. Zhang, G. Chen, *Energy Storage Mater.* **2021**, 38, 231.
- [25] X. Li, W. Lv, G. Wu, G. Fu, W. Zhang, Z. Li, *Chem. Eng. J.* **2021**, 426, 131899.
- [26] Zhang, B. Z., J. Li, J. Liu, X. Huo, F. Kang, *Chem. Eng. J.* **2021**, 403, 126377.
- [27] A. Lv, S. Lu, M. Wang, H. Shi, W. Yan, S. Jiao, *J. Energy Chem.* **2022**, 69, 35.
- [28] Q. Pang, J. Meng, S. Gupta, X. Hong, C. Y. Kwok, J. Zhao, Y. Jin, L. Xu, Z. Karahan, Z. Wang, S. Toll, L. Mai, L. F. Nazar, M. Balasubramanian, B. Narayanan, D. R. Sadoway, *Nature* **2022**, 608, 704.
- [29] W. Chu, S. He, S. Liu, X. Zhang, S. Li, H. Yu, *Chem. Commun.* **2022**, 58, 11539.
- [30] X. Zhang, M. Wang, J. Tu, S. Jiao, *J. Energy Chem.* **2021**, 57, 378.
- [31] M. Walter, K. V. Kravchik, C. Bofer, R. Widmer, M. V. Kovalenko, *Adv. Mater.* **2018**, 30, 1705644.
- [32] D. J. Kim, D. J. Yoo, M. T. Otle, A. Prokofjevs, C. Pezzato, M. Owczarek, S. J. Lee, J. W. Choi, J. F. Stoddart, *Nat. Energy* **2019**, 4, 51.
- [33] L. Zhou, Z. Zhang, L. Cui, F. Xiong, Q. An, Z. Zhou, X. F. Yu, P. K. Chu, K. Zhang, *Cell Rep. Phys. Sci.* **2021**, 2, 100354.
- [34] G. Wang, E. Dmitrieva, B. Kohn, U. Scheler, Y. Liu, V. Tkachova, L. Yang, Y. Fu, J. Ma, P. Zhang, F. Wang, J. Ge, X. Feng, *Angew. Chem., Int. Ed.* **2022**, 134, 202116194.
- [35] J. Tu, W. Wang, H. Lei, M. Wang, C. Chang, S. Jiao, *Small* **2022**, 18, 2201362.
- [36] T. Lu, Z. Zhang, B. Chen, S. Dong, C. Wang, A. Du, G. Cui, *Mater. Today Energy* **2020**, 17, 100450.
- [37] N. P. Stadie, S. Wang, K. V. Kravchik, M. V. Kovalenko, *ACS Nano* **2017**, 11, 1911.
- [38] C. Li, S. Dong, R. Tang, X. Ge, Z. Zhang, C. Wang, Y. Lu, L. Yin, *Energy Environ. Sci.* **2018**, 11, 3201.
- [39] J. Yang, M. A. Bisset, R. A. W. Dryfe, *ChemSusChem* **2021**, 14, 1700.
- [40] R. Yazami, Y. F. Reynier, *Electrochim. Acta* **2002**, 47, 1217.
- [41] T. Li, T. Cai, H. Hu, X. Li, D. Wang, Y. Zhang, Y. Cui, L. Zhao, W. Xing, Z. Yan, *J. Mater. Chem. A* **2022**, 10, 10829.
- [42] Y. Zheng, H. Wu, W. Yi, X. Lai, H. Dai, X. Han, M. Ouyang, *J. Power Sources* **2020**, 478, 229039.
- [43] S. Jiao, H. Lei, J. Tu, J. Zhu, J. Wang, X. Mao, *Carbon* **2016**, 109, 276.
- [44] J. Wang, J. Tu, C. Chang, H. Zhu, *J. Power Sources* **2021**, 492, 229674.
- [45] J. Shi, J. Zhang, J. Guo, *ACS Energy Lett.* **2019**, 4, 2124.
- [46] Y. Song, S. Jiao, J. Tu, J. Wang, Y. Liu, H. Jiao, X. Mao, Z. Guo, D. J. Fray, *J. Mater. Chem. A* **2017**, 5, 1282.
- [47] C. Y. Chen, T. Tsuda, S. Kuwabata, C. L. Hussey, *Chem. Commun.* **2018**, 54, 4164.
- [48] T. H. Kim, E. K. Jeon, Y. Ko, B. Y. Jang, B. S. Kim, H. K. Song, *J. Mater. Chem. A* **2014**, 2, 7600.
- [49] Y. Wen, K. He, Y. Zhu, F. Han, Y. Xu, I. Matsuda, Y. Ishii, J. Cumings, C. Wang, *Nat. Commun.* **2014**, 5, 4033.
- [50] M. A. Pimenta, G. Dresselhaus, M. S. Dresselhaus, L. G. Cancado, A. Jorio, R. Saito, *Phys. Chem. Chem. Phys.* **2007**, 9, 1276.
- [51] K. N. Kudin, B. Ozbas, H. C. Schniepp, R. K. Prud'homme, I. A. Aksay, R. Car, *Nano Lett.* **2008**, 8, 36.
- [52] M. Thommes, K. I. Kaneko, A. V. Neimark, J. P. Olivier, F. Rodriguez-Reinoso, J. Rouquerol, K. S. W. Sing, *Pure Appl. Chem.* **2015**, 87, 1051.
- [53] S. Guo, H. Yang, M. Liu, X. Feng, Y. Gao, Y. Bai, C. Wu, *ACS Appl. Mater. Interfaces* **2021**, 13, 22549.
- [54] C. Li, J. Patra, J. Li, P. C. Rath, M. H. Lin, J. K. Chang, *Adv. Funct. Mater.* **2020**, 30, 1909565.
- [55] C. Zhang, R. He, J. Zhang, Y. Hu, Z. Wang, X. Jin, *ACS Appl. Mater. Interfaces* **2018**, 10, 26510.
- [56] J. Kim, M. R. Raj, G. Lee, *Nano-Micro Lett.* **2021**, 13, 171.
- [57] J. Wei, W. Chen, D. Chen, K. Yang, *J. Mater. Sci. Technol.* **2018**, 34, 983.
- [58] H. Lei, J. Tu, Z. Yu, S. Jiao, *ACS Appl. Mater. Interfaces* **2017**, 9, 36702.
- [59] C. C. Chen, Sutarsis, J. P., F. M. Wang, J. Y. Lin, Q. F. Dong, Y. S. Su, J. K. Chang, *Carbon* **2023**, 204, 555.
- [60] M. Haque, Q. Li, C. Rigato, A. Rajaras, A. D. Smith, P. Lundgren, P. Enoksson, *J. Power Sources* **2021**, 485, 229328.
- [61] Y. Gao, C. Zhu, Z. Chen, G. Lu, *J. Phys. Chem. C* **2017**, 121, 7131.
- [62] X. Zhang, N. Sukpirom, M. M. Lerner, *Mater. Res. Bull.* **1999**, 34, 363.
- [63] J. K. Chang, I. W. Sun, S. J. Pan, M. H. Chuang, M. J. Deng, W. T. Tsai, *Trans. IMF* **2008**, 86, 227.
- [64] H. Wang, S. Gu, Y. Bai, S. Chen, N. Zhu, C. Wu, F. Wu, *J. Mater. Chem. A* **2015**, 3, 22677.
- [65] P. Bhauriyal, A. Mahata, B. Pathak, *Phys. Chem. Chem. Phys.* **2017**, 19, 7980.
- [66] M. Angell, G. Zhu, M. C. Lin, Y. Rong, H. J. Dai, *Adv. Funct. Mater.* **2020**, 30, 1901928.
- [67] G. Zhu, X. Tian, H. C. Tai, Y. Y. Li, J. Li, H. Sun, P. Liang, M. Angell, C. L. Huang, C. S. Ku, W. H. Hung, S. K. Jiang, Y. Meng, H. Chen, M. C. Lin, B. J. Hwang, H. Dai, *Nature* **2021**, 596, 525.

# ADVANCED FUNCTIONAL MATERIALS

## Supporting Information

for *Adv. Funct. Mater.*, DOI 10.1002/adfm.202305511

Self-Discharge Behavior of Graphitic Cathodes for Rechargeable Aluminum Batteries

*Chi Li, Yi-Xiu Chen, Jagabandhu Patra, Shi-Xian Lu, Chien-Te Hsieh, Chun-Chen Yang,  
Quan-Feng Dong, Ju Li and Jeng-Kuei Chang\**

## Supporting Information

**Self-Discharge Behavior of Graphitic Cathodes for Rechargeable  
Aluminum Batteries**

*Chi Li, Yi-Xiu Chen, Jagabandhu Patra, Shi-Xian Lu, Chien-Te Hsieh, Chun-Chen Yang,  
Quan-Feng Dong, Ju Li, Jeng-Kuei Chang\**

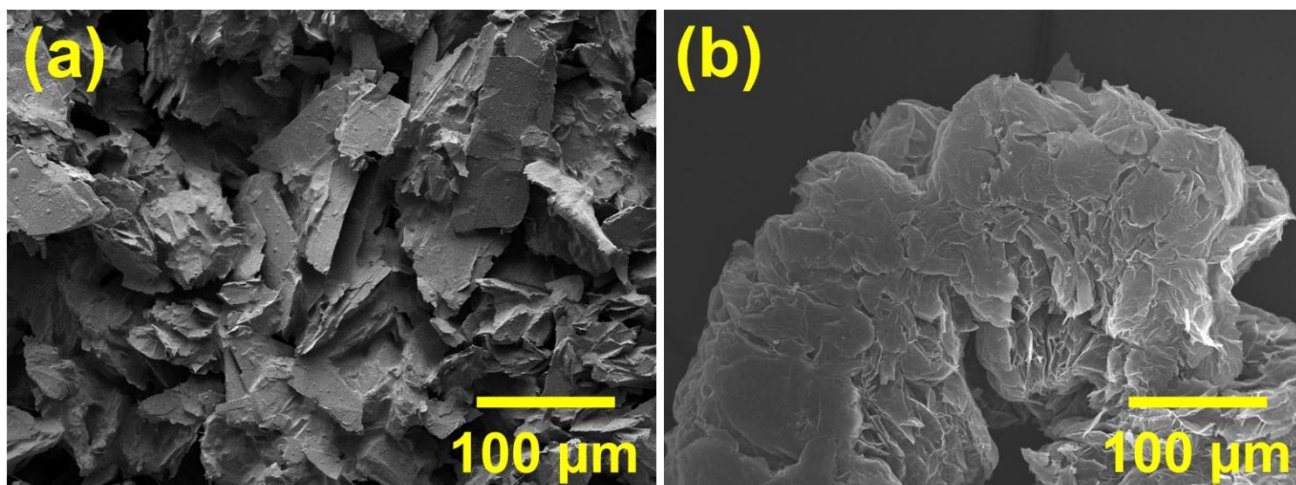


**Figure S1.** SEM images of (a) NG and (b) EG electrodes after 1000 charge-discharge cycles.

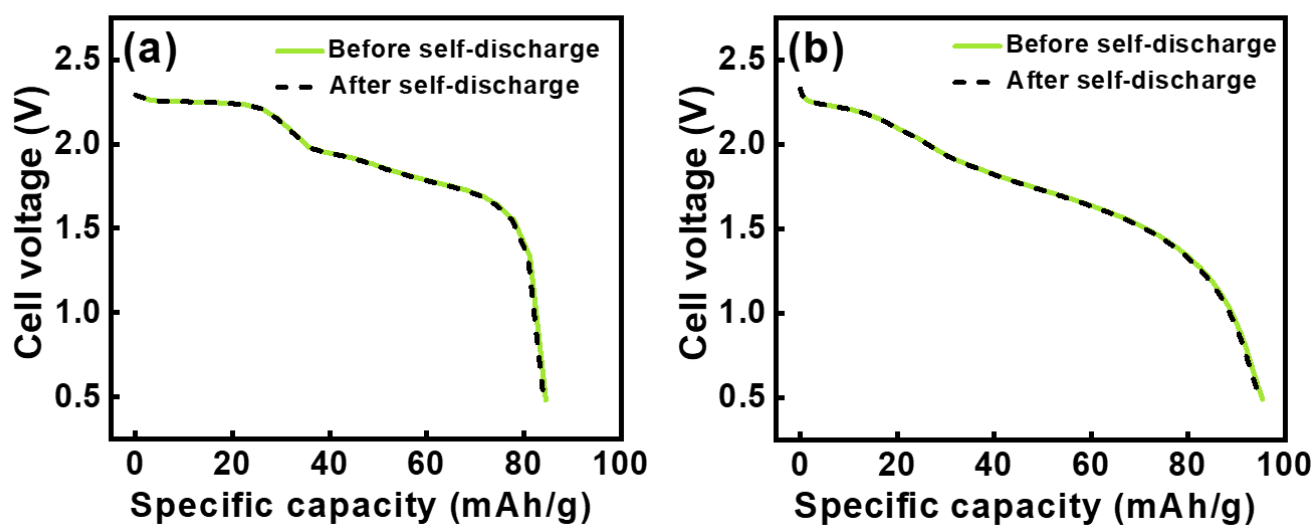


**Figure S2.** Discharge curves of (a) NG and (b) EG electrodes measured before and after the self-discharge cycles.

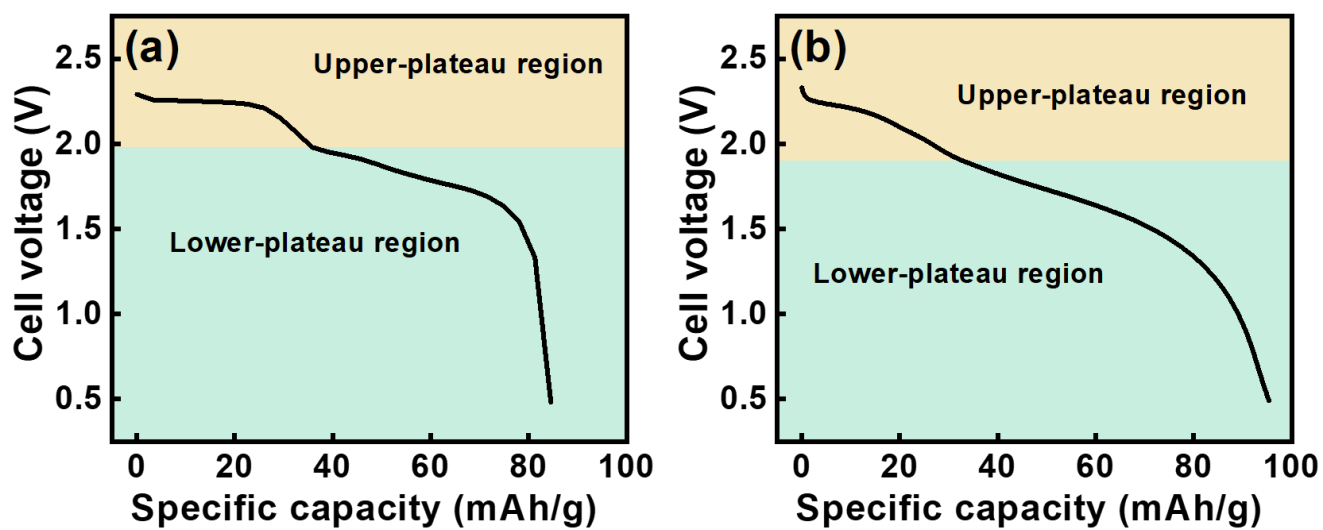


**Figure S3.** The upper-plateau and lower-plateau regions of (a) NG and (b) EG electrodes.

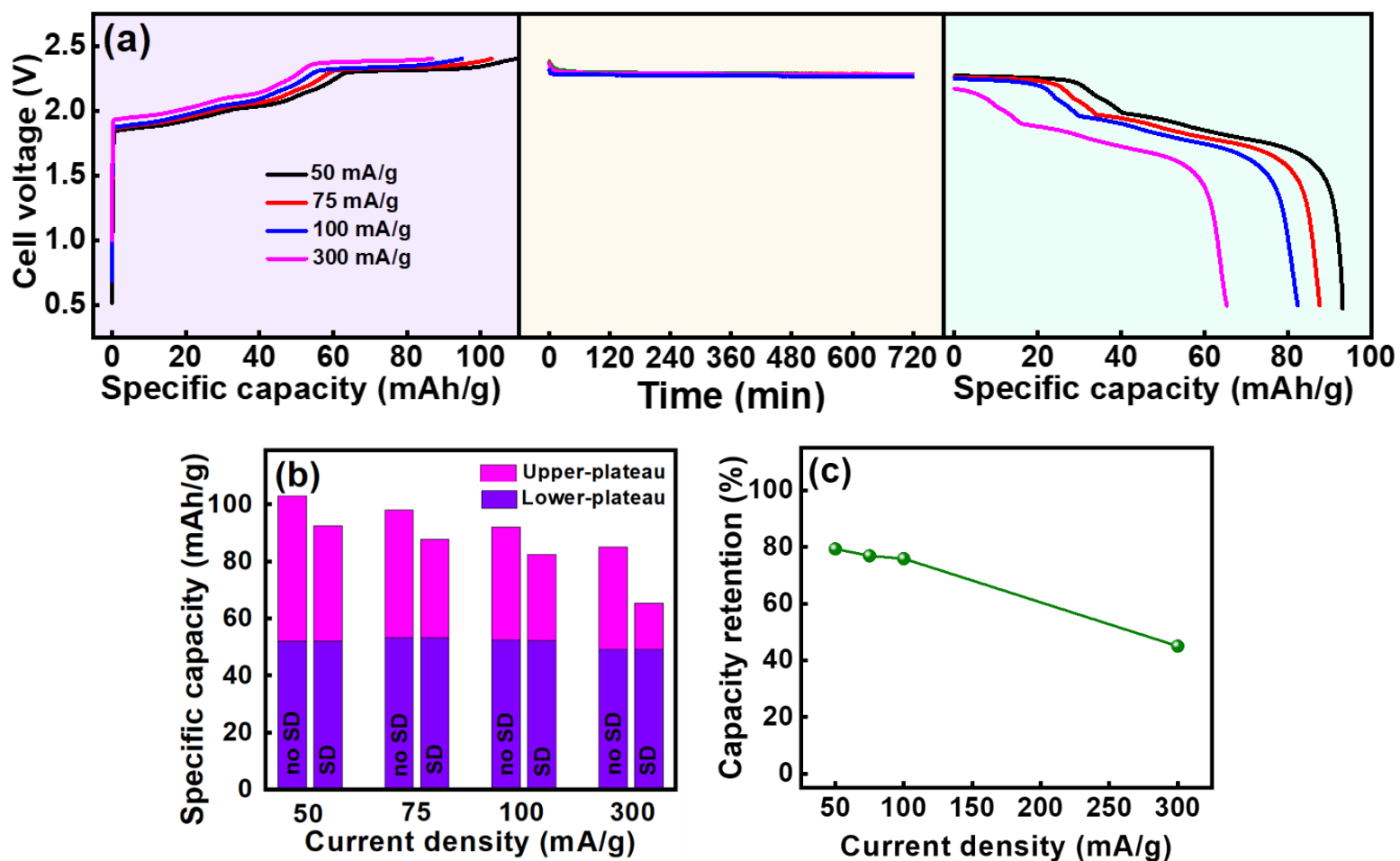


**Figure S4.** (a) Self-discharge properties of NG electrode measured at various rates. (b) Capacities of upper and lower plateaus for NG electrode measured with various rates before and after 12 h of self-discharge (SD). (c) Capacity retention of upper plateau of NG electrode measured with various rates after 12 h of self-discharge.

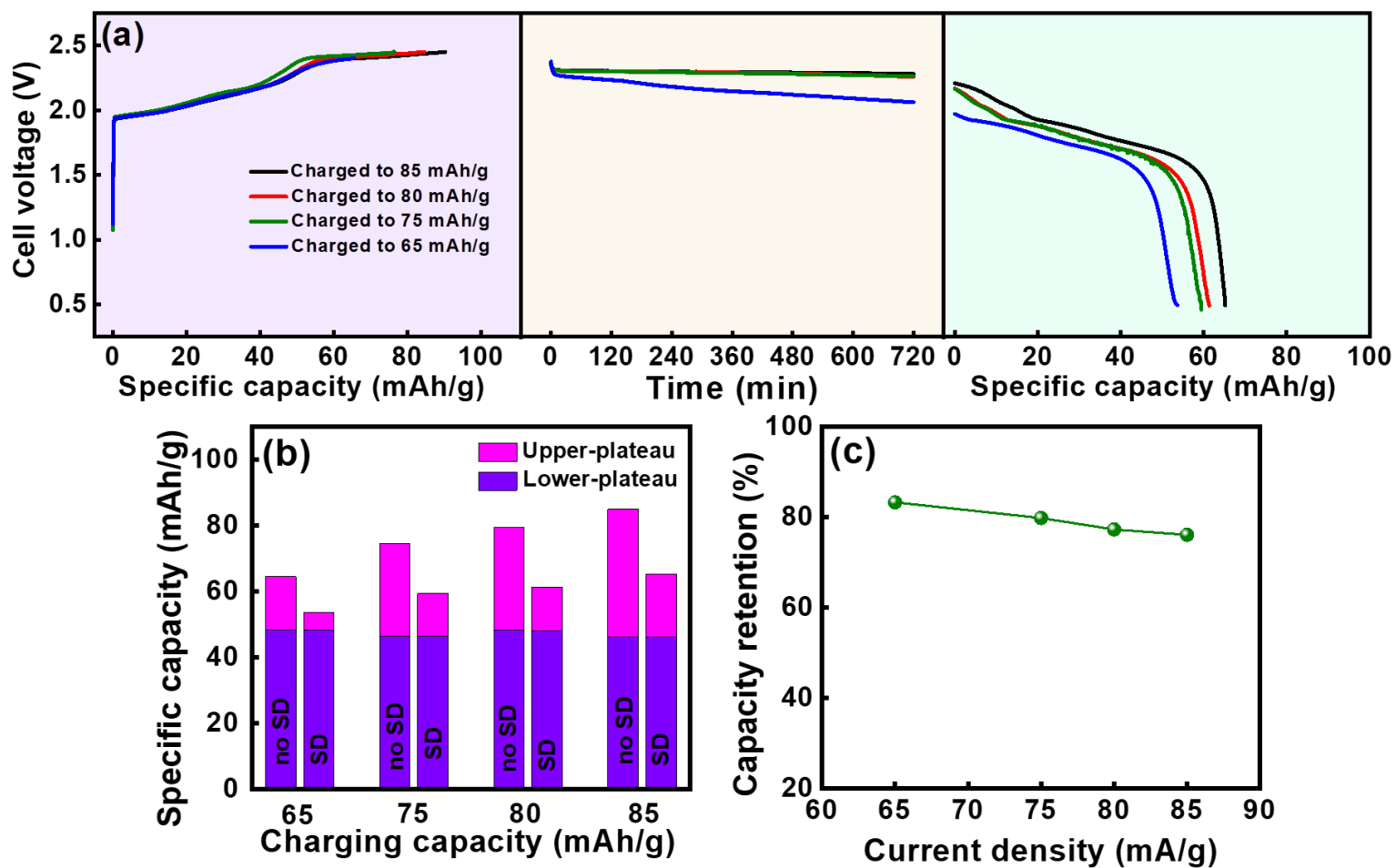


**Figure S5.** (a) Self-discharge properties of NG electrode charged up to various capacities. (b) Capacities of upper and lower plateaus for NG electrode charged up to various capacities before and after 12 h of self-discharge (SD). (c) Overall capacity retention of NG electrode charged up to various capacities after 12 h of self-discharge.

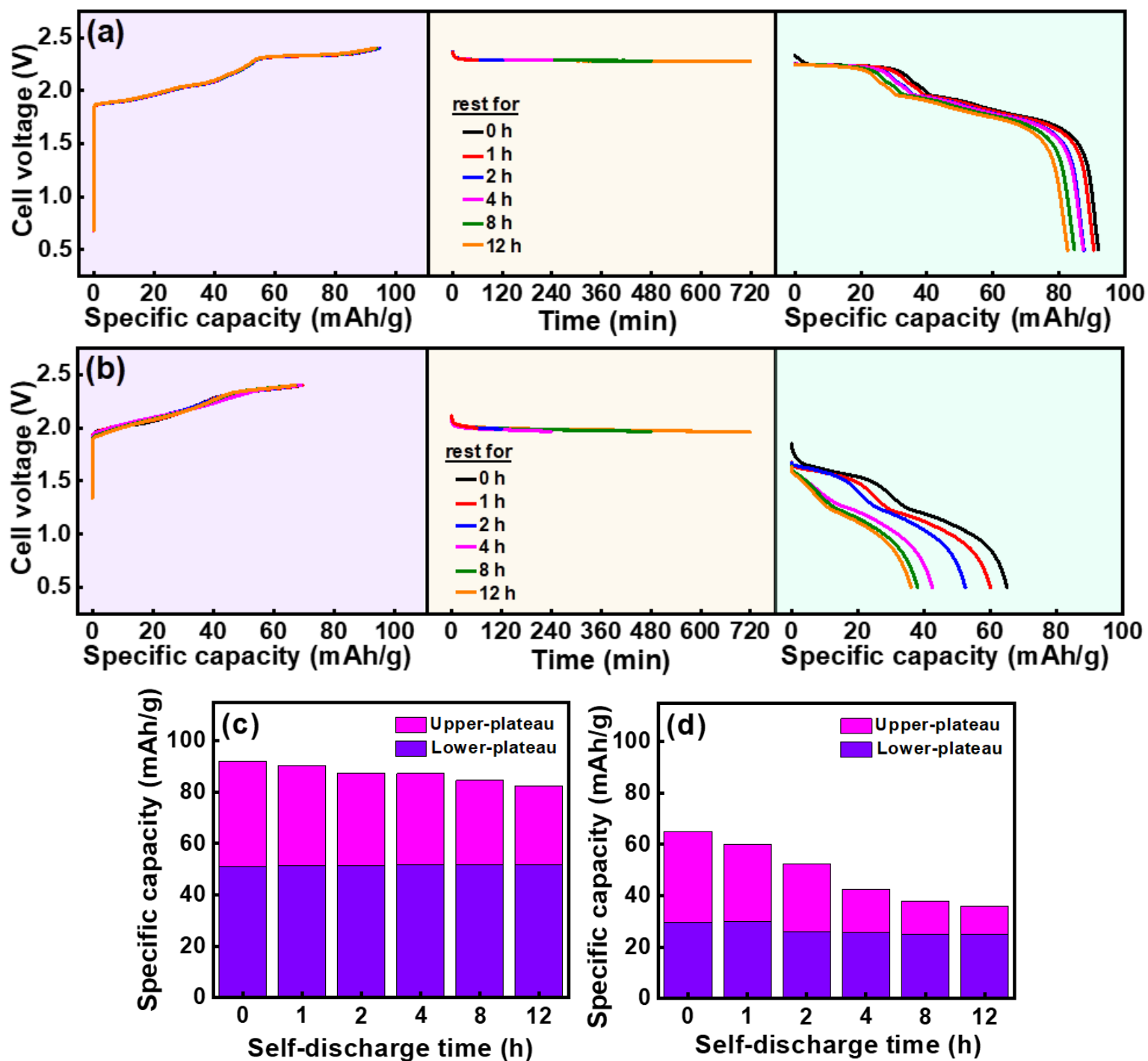


**Figure S6.** Self-discharge properties of NG electrodes measured at  $0.1 \text{ A g}^{-1}$  in (a) EMICl-AlCl<sub>3</sub> and (b) urea-AlCl<sub>3</sub> electrolytes. Capacities attributed to upper and lower plateaus of NG electrodes measured in (c) EMICl-AlCl<sub>3</sub> and (d) urea-AlCl<sub>3</sub> electrolytes after various durations of self-discharge.